# Bubble Proliferation or Dissolution of Cavitation Nuclei in the Beam Path of a Shock-Wave Lithotripter

Spencer Frank,[1] Jaclyn Lautz,[2] Georgy N. Sankin,[2,*] Andrew J. Szeri,[1,†] and Pei Zhong[2,‡]
[1]*Department of Mechanical Engineering, University of California, Berkeley, California 94720, USA*
[2]*Department of Mechanical Engineering and Materials Science, Duke University, Durham, North Carolina 27708, USA*

(Received 13 March 2014; revised manuscript received 29 September 2014; published 3 March 2015)

It is hypothesized that the decreased treatment efficiency in contemporary shock-wave lithotripters is related to tensile wave attenuation due to cavitation in the prefocal beam path. Utilizing high-speed imaging of the beam path and focal pressure waveform measurements, tensile attenuation is associated with bubble proliferation. By systematically testing different combinations of pulse-repetition frequency and gas concentration, we modulate the bubble-dissolution time to identify which conditions lead to bubble proliferation and show that reducing bubble proliferation in the beam path significantly improves acoustic transmission and stone comminution efficiency *in vitro*. In addition to experiments, a bubble-proliferation model is developed that takes gas diffusion across the bubble wall and bubble fragmentation into account. By aligning the model with experimental observations, the number of daughter bubbles produced after a single lithotripter bubble collapse is estimated to be in the range of $253 \sim 510$. This finding is on the same order of magnitude with previous measurements of an isolated bubble collapse in a lithotripter field by Pishchalnikov, McAteer, and Williams [BJU Int. 102, 1681 (2008)], and this estimate improves the general understanding of lithotripsy bubble dynamics in the beam path.

DOI: 10.1103/PhysRevApplied.3.034002

## I. INTRODUCTION

Shock-wave lithotripsy (SWL) is a nonsurgical procedure that utilizes high-energy focused shock waves to break up kidney stones [2]. Clinical experience has demonstrated that the treatment outcome of SWL depends critically on the design features and operating conditions of a lithotripter, with much emphasis given to the pulse-repetition frequency (PRF) [3–7]. Even a slight increase in the PRF from 1 to 2 Hz is shown to significantly decrease the effectiveness of treatment [8]. This result is attributed to cavitation effects in the beam path that cause significant tensile attenuation before the shock wave (SW) reaches the stone [9].

Cavitation bubbles produced in the beam path during SWL initially experience a large expansion, followed by a violent inertial collapse, leading to the formation of numerous daughter bubbles [10]. Whether the dissolution time of these daughter bubbles is greater or less than the time before the arrival of the next shock determines whether they can serve as cavitation nuclei themselves [11]. If the dissolution time of the daughter bubbles is less than the shock period (i.e., the inverse PRF) of delivered lithotripter pulses, then only cavitation nuclei stabilized on suspended dust particles [12] or the like may be present upon the arrival of the next shock wave. Under such a scenario, as is typical if the water is degassed, the number of viable cavitation nuclei may decrease, and *bubble reduction* may occur, which is a decrease in cavitation activity in the beam path as treatment progresses. In contrast, in nondegassed water, the dissolution time of daughter bubbles often exceeds the shock period when the PRF is greater than 1 Hz [13] and allows the remaining daughter bubbles to be viable cavitation nuclei for the ensuing shock [11]. In this case, *bubble proliferation* may occur [14–16], which leads to an enormous increase in cavitation activity in the beam path.

When bubble proliferation occurs in the beam path, the tensile component of the lithotripter pulse is attenuated due to loss of the tensile wave energy to expanding cavitation bubbles [1,5,9]. This tensile attenuation has been shown to depend on the density of cavitation nuclei in the beam path and is sensitive to the PRF [17]. Furthermore, if the tensile wave is attenuated before it reaches the stone, cavitation may decrease in the vicinity of the stone which may lead to a reduction in stone comminution [18].

Various methods have been tested that attempt to control bubble proliferation in the beam path by altering the cavitation threshold and/or decreasing the dissolution time of bubbles. To understand how the density of nuclei affect bubble proliferation, Arora, Ohl, and Lohse [17] inject artificial cavitation nuclei into the beam path and study the

*Corresponding author.
georgy.sankin@duke.edu
†aszeri@berkeley.edu
‡pzhong@duke.edu

 

bubble lifetime and the bubble cluster spatial properties. Henglein, Herburger, and Gutierrez [19] modulate the presence of cavitation nuclei by using ultrasound to destroy cavitation nuclei. Sapozhnikov *et al.* [11] show that cavitation activity in the beam path depends on overpressure and indirectly on gas concentration; the latter is because gas concentration is inversely proportional to hydrostatic pressure. Strasberg [20] tests the effects of various methods of water treatment on cavitation in water. His work shows in separate experiments that (i) increasing over pressure and (ii) decreasing the gas concentration had a similar effect in increasing the cavitation threshold. However, applying overpressure is shown to affect the cavitation threshold in a *path-dependent* manner. In contrast, lowering the gas concentration without altering the overpressure tends to follow a linear trend with lower gas concentrations increasing the cavitation threshold in a more predictable and repeatable manner. Because of this observation, in this work, rather than apply overpressure, we choose to instead only degas the water. In varying the gas content, we are able to repeatedly fit our experimental results to a simple model of bubble dissolution, as will be explained.

In this effort, we systematically investigate bubble dynamics in the beam path as they depend on the PRF and gas concentration. By performing this systematic investigation, a strong association between bubble activity and tensile attenuation is revealed, as well as the implications on stone comminution for an *in vitro* setup. Additionally, we choose to investigate the first five shocks in order to gain insight into how bubble activity and tensile attenuation initially evolve from shock to shock, rather than in treatment at the steady state such as in the work by Sapozhnikov *et al.* [11].

The experimental data obtained in this work are also useful in that they can provide evidence of the plausibility of bubble dynamic models in which the gas concentration and PRF are parameters of interest. We make direct use of our observations by developing a simple model of bubble dissolution that accounts for fragmentation. This model expands on previous work in modeling bubble dissolution [11], in that it accounts for the fragmentation of bubbles. This expansion is an important addition; fragmentation can significantly affect dissolution time, because the smaller daughter bubbles born in a violent collapse dissolve much more rapidly than the larger bubbles would if they did not collapse. The estimate of the number of daughter bubbles obtained from the model agrees with previous observations [16] and provides some insight into the bubble dynamics in the beam path during SWL.

The paper is organized as follows: first, we describe our experimental setup. Results of the experiments show that increased cavitation activity along the beam path is associated with attenuation of a lithotripter shock wave (LSW), which has implications on *in vitro* stone comminution efficiency. Next, a straightforward model is developed that involves bubble fragmentation and gas diffusion, as they depend on gas concentration. Finally, the results of the experiments and the model are discussed and conclusions are drawn.

## II. MATERIALS AND METHODS

### A. Experimental apparatus and degassing system

The experimental setup [Fig. 1(a)], used previously in Ref. [18], includes an electromagnetic shock-wave source (focal length $F = 181.5$ mm) mounted to the bottom of a 40-l acrylic tank filled with partially degassed water of varying oxygen concentrations ($c = 2.05$–$7.5$ mg/l). This setup represents an *in vitro* setting, with a clear homogenous beam path that is unobstructed. With this *in vitro* setup, we have the ability to control the gas concentration in the beam path.

A gas exchange unit (G453 Liqui-Cel® Membrane Contactor, Membrana GmbH) is used to remove dissolved gases from the water through a hydrophobic polypropylene membrane with a pore size of 0.5 $\mu$m, aided by a vacuum pump (1VBF-26-M100X, Marathon Electric, Wausau, WS). The oxygen concentration in the water is monitored during the experiment by using an electrochemical oxygen meter (ExStik II, Extech Instruments Corp.). At a flow rate of 20 $cm^3/s$, the degassing system can reduce the oxygen concentration in the tank to approximately 2 mg/l (degassed water) in about 30 min. When such degassed water is kept in the tank overnight, the oxygen concentration increases to approximately 4 mg/l. In this study, three levels of oxygen concentrations in the water ($c = 2.05$, 4.30, and 7.5 mg/l) are prepared and used for experiments. The corresponding nondimensional gas concentration is $f = c/c_{sat} = 0.24$, 0.49, and 0.86 with $c_{sat} = 8.72$ mg/l $O_2$ at 295 K [21].

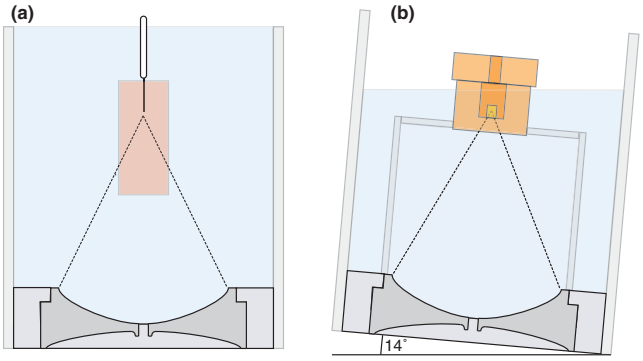


FIG. 1. (a) Experimental setup of free-field lithotripter used for high-speed imaging and pressure waveform measurements. The shaded region indicates the field of view of the high-speed camera. (b) Stone comminution setup with polyurethane stone holder. Water in the tank is filtered and degassed, while water inside of stone holder is from the tap. Focal length $F = 181.5$ mm.

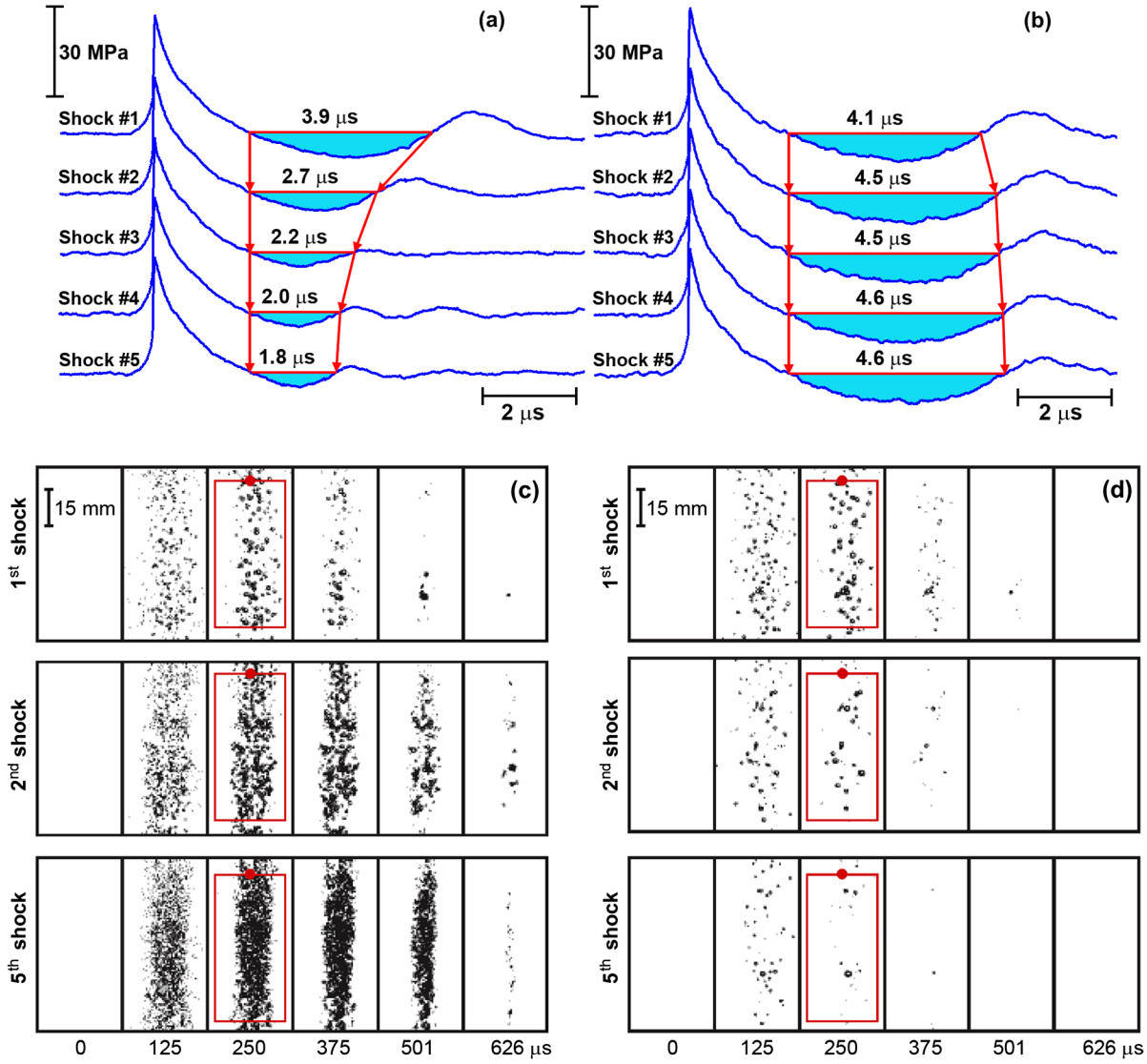


FIG. 2. The pressure waveforms (a),(b) measured in free field and corresponding representative high-speed images (20-$\mu$s exposure time) of cavitation activity (c),(d) for the first five consecutive shocks delivered at a PRF = 1 Hz in (a),(c) nondegassed water ($f = 0.86$) and (b),(d) degassed water ($f = 0.24$). The tensile phase (shaded) is attenuated from the first to fifth shocks in nondegassed water (a) and strengthened in degassed water (b). Concomintantly, cavitation activity increases in nondegassed water (c) and reduces in degassed water (d). The cavitation index is quantified at maximum cavitation activity ($t = 250$ $\mu$s) within the prefocal area (30 mm in width, 70 mm in height) with the dot showing the location of the lithotripter focus and the hydrophone position.

### B. Cavitation analysis

Cavitation along the lithotripter beam path is captured by using a high-speed camera (Phantom 7.3, Vision Research Inc.) at a frame rate of 23 000 frames/s with an exposure time of 20 $\mu$s. A 55-mm lens ($f/2.8$, Micro-Nikkor, Nikon Corp.) is used, providing a resolution of 3.4 pixels/mm and a depth of field greater than 20 mm. The camera is externally triggered by a digital delay-pulse generator (565-2C-H-E, Berkeley Nucleonics Corp.) and records 20 frames per lithotripter shock over a 900-$\mu$s time interval. A continuous 84-W white LED diffuser panel (60 × 60 cm, width × height, HCL-FLT8N-0600A0-F1, ATG Electronics Corp.) is used to provide backlight illumination and to aid in keeping the water temperature in the range of 21.1–23.5° C during the experiment.

Imaging data are analyzed by converting gray-scale images into binary images (black and white) to isolate bubble boundaries in MATLAB (R2012b, the MathWorks Inc.) following a previously described protocol [18]. The cavitation index $C_{\mathrm{ind}}$ is calculated by measuring the total area of bubbles in a specified region of interest. The data from the first five consecutive shocks are analyzed in a prefocal rectangular area (30 × 70 mm,width × height) and averaged from data obtained in five samples.

### C. Pressure waveform measurements

During cavitation imaging, a fiber-optic hydrophone (FOPH-500, RP Acoustics, Leutenbach, Germany) is used to measure the pressure pulse delivered to the lithotripter focus using a digital oscilloscope (6050A WaveRunner, LeCroy Inc.) operated at a 500-Msamples/s sampling rate. The lithotripter, oscilloscope, and high-speed camera are simultaneously triggered at a PRF of 0.5, 1, 2, or 3 Hz by using a multichannel digital delay-pulse generator (565-2C, Berkeley Nucleonics Corp.). In each case, pressure waveforms are recorded for the first five consecutive lithotripter pulses.

Pressure waveforms are postprocessed to assess the attenuation of the shock wave by applying a moving average filter with 0.2-$\mu$s time window. Although smoothing the waveform may decrease the amplitude of the shock front, it has minimal effect on the tensile wave to be evaluated. Tensile phase duration $t_-$ is defined by the time between the two zero-crossing points [Figs. 2(a) and 2(b)]. Furthermore, the pressure impulse $P_I$ is computed by using

$$P_I = \int_{t_-} p(t)dt, \tag{1}$$

where $p(t)$ is the measured pressure waveform. This measure facilitates a comparison of the pressure waveforms and their corresponding cavitation potential [22] at different experimental conditions. Under each condition, four pressure waveforms are averaged that do not exhibit noticeable cavitation-related artifacts [23].

### D. Stone comminution

*In vitro* stone comminution experiments are performed in a water tank tilted at 14° [Fig. 1(b)] to prevent bubbles from accumulating beneath the stone holder. Stones are treated in a stone holder [Figs. 1(b) and 7(a), highlighted with a dashed line] made of polyurethane rubber (part A is prepolymer, B, polyol, and C, softener, Polytek Development Corp., Easton, PA, USA) at a 1:1:1 mixing ratio. The resulting material has similar acoustic properties (sound speed $C = 1.4$ km/s, density $\rho = 1.1$ g/cm$^3$) to those of biological tissues. The shock-wave source is operated at an energy setting of $E = 3.2$ to produce a $p_+ = 41$ MPa inside the stone holder during comminution experiments. Cylindrical stone phantoms of 9 mm × 10 mm (width × height) are made of calcium sulfate (BEGO, Smithfield, RI) and water at a 5:2 (powder-to-water) mixing ratio, corresponding to a longitudinal wave speed $C_L = 3.1$ km/s and $\rho = 1.6$ g/cm$^3$ [24].

The coupling fluid conditions are either degassed water ($c = 2.3$ mg/l $O_2$) or nondegassed water ($c = 7.2$ mg/l $O_2$). The stone holder is filled with tap water ($c = 7.2$ mg/l $O_2$) to simulate *in vivo* cavitation conditions in the vicinity of the stone [25]. After stones are treated with 250 shocks at 1 Hz, the fragments are collected and dried for 24 h in an oven at 40°C. Large fragments are separated by using a 2.0-mm sieve (No. 10, W. S. Tyler, Mentor, OH).

## III. EXPERIMENTAL RESULTS

### A. Tensile phase dynamics and associated cavitation activity

Acoustic-field measurements demonstrate the effect of gas concentration and the PRF on tensile phase attenuation. The pressure waveforms of the first five shocks delivered at a 1-Hz PRF in nondegassed water ($f = 0.86$) and degassed water ($f = 0.24$) are shown in Figs. 2(a) and 2(b), respectively. From the first to the fifth shock, $t_-$ decreases from 3.9 to 1.8 $\mu$s in nondegassed water, indicating an attenuation of the tensile wave. In contrast, $t_-$ marginally increases from 4.1 to 4.6 $\mu$s in degassed water, indicating an improved transmission of the tensile wave.

These two distinct and opposite trends become more apparent when comparing the pressure impulse ratio $T$ in each case given by

$$T = \frac{P_I(\text{fifth shock})}{P_I(\text{first shock})}, \tag{2}$$

where $T < 1$ indicates attenuation and $T > 1$ corresponds to intensification of the tensile wave. Figures 3(a)–3(c) show the progression of the pressure impulse for five consecutive shocks at different PRFs and gas concentrations. In nondegassed water [Fig. 3(a), $f = 0.86$], $P_I$ decreases sharply from the first to the fifth shock, indicating significant attenuation of the tensile wave for all cases, similar to the previous observation by Pishchalnikov, McAteer, and Williams [1]. At the lowest PRF = 0.5 Hz, $P_I$ decreases from 21.2 to 9.9 Pa s ($T = 0.47$). At the highest PRF = 3 Hz, $P_I$ decreases even further to 1.8 Pa s ($T = 0.09$), an enormous attenuation. For partially degassed water [Fig. 3(b), $f = 0.49$], there is significant attenuation of the tensile wave at higher PRFs (i.e., $T = 0.47$ for PRF = 2 Hz and $T = 0.13$ for PRF = 3 Hz). In contrast, a marginal intensification of the tensile phase is observed at lower PRFs (i.e., $T = 1.03$ for PRF = 1 Hz and $T = 1.10$ for PRF = 0.5 Hz). Of particular interest are the results obtained at PRF = 2 Hz, where $P_I$ is found to change slowly, suggesting a transition across the threshold from attenuation to intensification. Finally, in the degassed case, [Fig. 3(c), $f = 0.24$], it is observed that degassing the water in the beam path effectively eliminates tensile wave attenuation ($T = 1.13$–$1.23$) for all PRFs evaluated.

Similar to the distinct changes in the pressure waveforms shown in Figs. 2(a) and 2(b), there are differing trends in the changes of cavitation activities as shown in Figs. 2(c) and 2(d). Each row in these representative images shows the time history of bubble expansion and collapse produced by a single shock. For each shock, the cavitation index

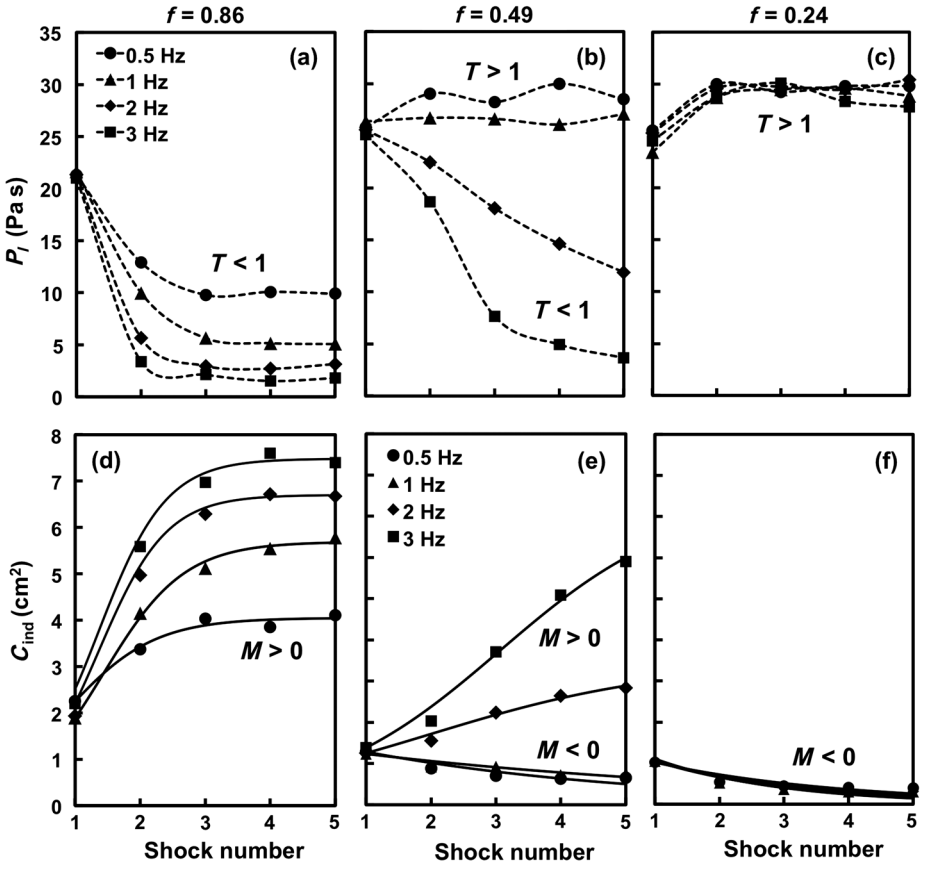


FIG. 3. Pressure impulse (a)–(c) and cavitation index (d)–(f) for the first five consecutive shocks delivered at PRFs of 0.5 (circles), 1 (triangles), 2 (diamonds), and 3 Hz (squares) in water with gas concentration $f = 0.86$ (a),(d), 0.49 (b),(e), and 0.24 (c),(f). Theoretical curves (solid lines) are superimposed over the experimental data in (d)–(f) with best-fitting parameters listed in Table I.

$C_{\text{ind}}$ is quantified at maximum bubble activity [$t = 250$ $\mu$s, shown with a red box in the third frame of Figs. 2(c) and 2(d)]. By evaluating the value of $C_{\text{ind}}$ from the first to the fifth shock, either bubble proliferation [Figs. 2(c) and 3(d)] or bubble reduction [Figs. 2(d) and 3(f)] is observed.

In nondegassed water [Fig. 3(d), $f = 0.86$], $C_{\text{ind}}$ increases from 2.5 to 3.9 cm$^2$ at PRF = 0.5 Hz, and further to 7.2 cm$^2$ for PRF = 3 Hz, indicating strong bubble proliferation for all PRFs tested. In partially degassed water [Fig. 3(e), $f = 0.49$] at PRF = 3 Hz ($C_{\text{ind}}$ increasing from 1.3 to 5 cm$^2$) and at PRF = 2 Hz ($C_{\text{ind}}$ increasing from 1.3 to 2.9 cm$^2$), there is bubble proliferation. At lower PRFs, there is a transition to bubble reduction with $C_{\text{ind}}$ decreasing from 1.2 to 0.7 cm$^2$ for PRFs = 1 and 0.5 Hz. In degassed water [Fig. 3(f), $f = 0.24$], bubble reduction is observed for all the PRFs tested ($C_{\text{ind}}$ decreasing from 1.0 to 0.4 cm$^2$).

Figure 4 plots a proxy of bubble activity ($C_{\text{ind}}$) versus a proxy of tensile attenuation ($P_I$) to quantify how these two phenomena relate to each other. In general, Fig. 4 shows an inverse relationship between $C_{\text{ind}}$ and $P_I$ (i.e., increasing cavitation activity corresponds to a decreasing pressure

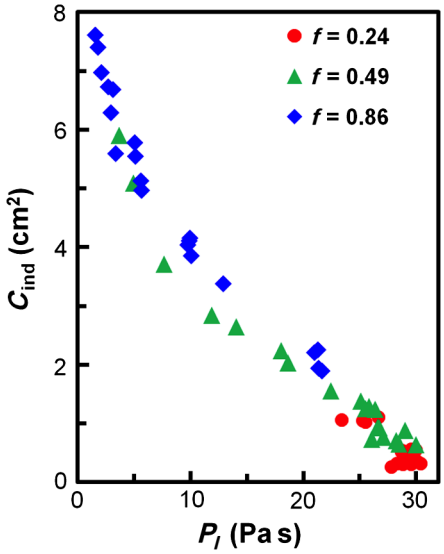


FIG. 4. Association between the cavitation index and pressure impulse. All the points appear to fall on a single curve, indicating that there is a direct relationship between cavitation and tensile attenuation regardless of the gas concentration, operating condition, and mechanism of bubble instigation.

TABLE I. The critical number of bubble fragments $\gamma_{cr}$ (theory), the bubble growth rate $M$ (experiment), and the acoustic transmission coefficient $T$ (experiment) for different $f$ and PRF. The greatest $\gamma$ $(= 253)$ with bubble reduction $(M < 0)$ and the smallest $\gamma$ $(= 510)$ with bubble proliferation $(M > 0)$ are starred.

| | $f = 0.86$ | | | $f = 0.49$ | | | $f = 0.24$ | | |
|---|---|---|---|---|---|---|---|---|---|
| PRF (Hz) | $\gamma_{cr}$ | $M$ | $T$ | $\gamma_{cr}$ | $M$ | $T$ | $\gamma_{cr}$ | $M$ | $T$ |
| 0.5 | $>10^3$ | 1.32 | 0.46 | 64 | −0.12 | 1.10 | 18 | −0.34 | 1.17 |
| 1.0 | $>10^3$ | 1.52 | 0.23 | 181 | −0.11 | 1.03 | 49 | −0.46 | 1.23 |
| 2.0 | $>10^3$ | 1.83 | 0.15 | 510* | 0.37 | 0.47 | 138 | −0.41 | 1.20 |
| 3.0 | $>10^3$ | 1.78 | 0.09 | $>10^3$ | 0.67 | 0.13 | 253* | −0.53 | 1.13 |

impulse of the tensile wave). Furthermore, all data points appear to fall on a single curve, indicating that the association between $P_1$ and $C_{ind}$ is independent of gas concentration $f$ and PRF.

### B. Identifying bubble proliferation or reduction

The cavitation data are fitted to a model of bubble concentration dynamics from Ref. [26] which was modified to the following equation:

$$\frac{dN}{ds} = MN - kN^2, \tag{3}$$

where $N$ is the number of bubbles and $s$ is the shock number. The first term on the right-hand side of Eq. (3) describes bubble multiplication with growth rate $M$. The second term describes bubble coalescence with the rate constant $k > 0$, which is insignificant in cases where bubble coalescence does not readily occur such as in a sparse bubble cloud. Following Margulis [26] and neglecting triple collisions, we further assume coalescence is proportional to $N^2$. Assuming that the number of bubbles after the first shock is $N(0) = N_0$, Eq. (3) can be solved for the number of bubbles $N(s)$ after the $s$th shock, given by

$$N(s) = N_0 \frac{e^{Ms}}{1 + \frac{kN_0}{M}(e^{Ms} - 1)}. \tag{4}$$

For a sparse bubble cloud, we assume that the overlap of bubbles should not be significant in the captured images. Thus, $N$ should be approximately proportional to the cavitation index for cases of a sparse bubble cloud (i.e., the first and second shocks for all cases, before the bubble density has become large and also in the cases of bubble reduction). With these assumptions we apply the model equation to all our cases and fit the coefficients. This model is by no means a precise or accurate fit model for all of the cases; it is only a way to identify when bubble proliferation $(M > 0)$ or bubble reduction $(M < 0)$ has taken place. The fitting curves are plotted over the cavitation data in Figs. 3(d)–3(f) with the respective best-fitting parameters shown in Table I.

Figure 5(a) shows the resulting $M$ parameter from the curve fitting of Eq. (4) for each experimental condition. In degassed water, $M$ is negative (reduction), and, hence, there are far fewer bubbles after five shocks [i.e., $N(5) \approx 0$ for all PRFs] [Fig. 5(b), third row]. In nondegassed water [Fig. 5(b), first row], $M$ is positive (proliferation) with

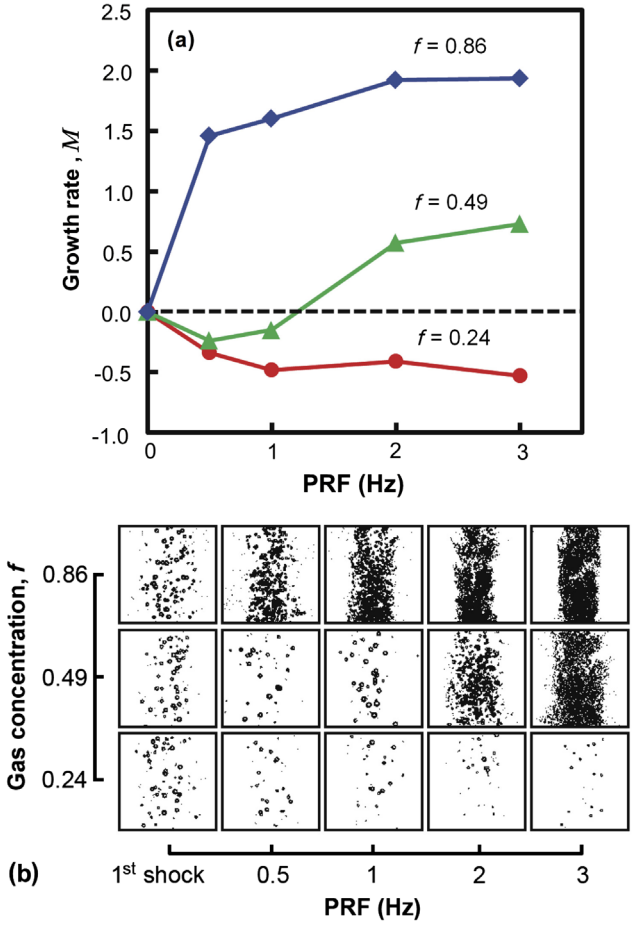


FIG. 5. (a) Cavitation growth rate as a function of PRF and gas concentration and (b) corresponding high-speed images (30 mm in width, 30 mm in height, 20-$\mu$s exposure time) of maximum cavitation activity showing the first shock (column 1) and the fifth shock (columns 2–5) for each PRF of 0.5, 1.0, 2.0, and 3.0 Hz. It can be seen that cavitation activity decreases for some cases $(M < 0)$ and increases for others $(M > 0)$.

nearly constant cavitation activity after the fifth shock [i.e., $N(5) \approx M/k$], representing an asymptotic solution of Eq. (4). In partially degassed water [Fig. 5(b), second row], two scenarios are possible, i.e., bubble proliferation ($M > 0$) for PRF $\geq 2$ Hz and bubble reduction ($M < 0$) for PRF $\leq 1$ Hz.

## IV. MODEL OF BUBBLE FISSION AND DISSOLUTION

To explain why under certain conditions bubbles proliferate and under other conditions there is a bubble reduction, we construct an estimate based on

$$\alpha = t_d/\mathrm{PRF}^{-1}, \tag{5}$$

which determines whether daughter bubbles can serve as cavitation nuclei for the next shock. $t_d$ is the dissolution time of daughter bubbles produced after collapses which depends on the dissolved gas concentration $c_\infty$. Specifically, if the dissolution time is greater than the period between shocks ($\alpha > 1$), then the surviving bubbles can act as cavitation nuclei for the next shock, which leads to *bubble proliferation*, with the number of bubbles rapidly increasing from shock to shock. On the other hand, if $\alpha < 1$, then bubbles do not survive till the next shock and instead a *reduction of bubbles* occurs, with numbers slowly decreasing—possibly due to the depletion of viable nuclei stabilized on dust particles; however, an examination of that mechanism is beyond the scope of the current work.

To estimate $t_d$ we use a model based on diffusion of noncondensable gas into a large cavitation bubble. This model, proposed by Akhatov *et al.* [27], estimates the mass of noncondensable gas (e.g., air) diffused into a bubble upon its initial expansion phase. The model starts with the spherical diffusion equation and assumes a single bubble in a quiescent liquid, with an exponentially decreasing gas concentration from the bubble wall to the ambient. After volume and time integration, an upper estimate for the mass $m_g$ of noncondensable gas taken up into a bubble upon its initial expansion is found as follows:

$$m_g \approx 4\sqrt{2}\pi R_{\max}^2 c_\infty \sqrt{D\tau}, \tag{6}$$

where $D$ is the diffusion coefficient of air in water ($D = 2.42 \times 10^{-9}$ m$^2$/s), $R_{\max}$ is the maximum radius of the bubble upon initial expansion, and $\tau$ is the collapse time. This derivation, which is shown in detail in Ref. [27], assumes that, because $m_g$ is proportional to $R^2$ and $R$ is large for most of its initial expansion, we may treat $R$ as a constant, $R_{\max}$, rather than a temporally varying radius function. Thus, Eq. (6) gives an upper bound for the amount of noncondensable gas inside a single lithotripter bubble after its initial expansion.

Approximate measurements from high-speed images are used to estimate the radius $R_{\max}$ of the largest bubble in the cluster in the range from 1 to 1.4 mm. A nominal value of $R_{\max} = 1.2$ mm is selected for calculations. A collapse time of $\tau \approx 400$ $\mu$s is measured for the largest bubbles, which is about 80% greater than the calculated double Rayleigh collapse time. This discrepancy in collapse time is also observed by Arora, Junge, and Ohl [28] and can be attributed to the prolongation of collapse time associated with near-field bubble-bubble interactions.

The mass within a small daughter bubble can be estimated by utilizing estimates for the mass of noncondensable gas $m_g$ diffused into a single large LSW-generated bubble. We shall assume that all the condensable gas (water vapor) within a bubble condenses comparatively rapidly upon collapse and fragmentation [29], as the vapor quickly condenses on the bubble surface with a time scale much smaller than the dissolution time of a bubble. Thus, for almost the entire bubble-dissolution process, the bubble effectively contains only noncondensable gas ($m_g \gg m_{\mathrm{vapor}}$ only 1 ms after collapse [29]).

It is worth noting that we are not attempting to model bubble collapse. Our primary concern is to estimate the amount of noncondensable gas within a single large LSW-generated bubble. This mass, after collapse, we postulate to be distributed among the smaller daughter bubbles, thus determining their size and subsequently their dissolution time, as will be explained.

Assuming only noncondensable gas remains shortly after collapse and fragmentation, we can estimate the size of a daughter bubble. Absent data on daughter-bubble size distribution, we assume that all bubbles are of equal size. To this end, we divide $m_g$ by the number of daughter bubbles $\gamma$ to determine the mass of gas within a single representative daughter bubble:

$$m_{g\gamma} = \frac{m_g}{\gamma}. \tag{7}$$

It is known that daughter bubbles exhibit a distribution of sizes, but it can be assumed that the smallest of the daughter bubbles would dissolve shortly after collapse, leaving behind the larger bubbles. This result effectively reduces the number of bubbles that would be available to serve as cavitation nuclei for the next shock. The value of $\gamma$ that is determined from the model would thus be an upper estimate of the number of daughter bubbles that would survive until the next shock.

The parameter $\gamma$ is unknown, but estimates of its order of magnitude have been previously measured. Pishchalnikov, Williams, and McAteer [16] estimate that $\gamma$ is on the order of $10$–$10^2$; however, for dense bubble clouds, the value of $\gamma$ is not clear due to attendant difficulties in imaging. Also, according to Ref. [27], bubble collapse and fragmentation may be dependent on the gas concentration in the surrounding fluid. Our model does not attempt to model collapse and does not take this dependence on gas concentration into

account. Rather, we circumvent this dependence by solving for $\gamma$ by forcing our model to agree with experimental results.

Subsequent to estimating the mass of gas within a daughter bubble, we use the ideal gas law to determine the daughter-bubble radius

$$P_0 \frac{4}{3}\pi r^3 = m_{g\gamma} R_{\text{gas}} T, \tag{8}$$

where $r$ is the daughter-bubble radius, $R_{\text{gas}} = 287$ J/kg K is the specific gas constant for air, $P_0 = 101\,325$ Pa is the static pressure away from the bubble, and $T = 295$ K is the water temperature.

After determining $r$, the associated dissolution time is calculated after Ref. [30] as follows:

$$t_d = \frac{r^2}{2Dd(1-f)}, \tag{9}$$

where $f$ is defined as the ratio of the gas concentration in the solution to the saturated gas concentration and $d$ is the ratio of the saturated dissolved gas concentration to the gas density, $d = c_{\text{sat}}/\rho_a = 0.02$. The findings by Epstein and Plesset [30] show that surface tension has a small effect ($< 20\%$) on the dissolution time for bubbles in the range of 1–10 $\mu$m when there are low gas concentrations ($f = 0.24$ and 0.49). For higher gas concentrations ($f = 0.86$), the effect of surface tension can cut the dissolution time in half. However, accounting for the effects of surface tension would not necessarily increase accuracy because of the many other assumptions. Since the primary goal of this model is to relate bubble-dissolution time to $\gamma$ and $f$, a dissolution time within the correct order of magnitude is considered acceptable.

A convenient form of the dissolution equation can be found by substituting Eqs. (6)–(8) into Eq. (9):

$$t_d = \left(\frac{f}{\gamma}\right)^{2/3} \frac{1}{1-f} \left[\sqrt{\frac{\tau}{d}} \frac{3R_{\max}^2 R_{\text{gas}} T \rho_a}{2DP_0}\right]^{2/3}. \tag{10}$$

The third factor in Eq. (10) is essentially a constant in our experiment of constant temperature and lithotripter energy settings, and thus $t_d$ can be thought of as a function of the number of daughter bubbles $\gamma$ and the gas concentration $f$.

## V. RESULTS OF DISSOLUTION MODEL

The only unknown parameter in Eq. (10) is $\gamma$, the number of daughter bubbles. To estimate $\gamma$, we align our dissolution equation to experimental observations. In order to do this, we follow the reasoning behind Eq. (5), and we say that there is a critical PRF (denoted $\text{PRF}_{\text{cr}}$) that will allow for exactly enough time for the bubbles to completely dissolve before the arrival of the next shock, corresponding to an $\alpha = 1$. This PRF can be written as

$$\text{PRF}_{\text{cr}} = 1/t_d(f,\gamma). \tag{11}$$

This curve is plotted in Fig. 6(a) versus $\gamma$ for each gas concentration.

Now, in examining Fig. 6(a), we can use the following experimental observations to determine a range for the number of daughter bubbles produced after a single-bubble collapse:

(i) For $f = 0.24$ bubble reduction is observed for all PRFs tested. This result means that $\text{PRF}_{\text{cr}}$ must be at least 3 Hz or greater; if it is any less than 3 Hz, then we would see bubble proliferation. With this reasoning, $\gamma$ at which our $f = 0.24$ curve crosses the 3-Hz horizontal line is the minimum $\gamma(= 253)$ that would cause our dissolution model to agree with experimental observation.

(ii) For $f = 0.49$ bubble reduction gives way to bubble proliferation between a PRF = 1 and 2 Hz. This result means that $\text{PRF}_{\text{cr}}$ must be at most 2 Hz; if it is

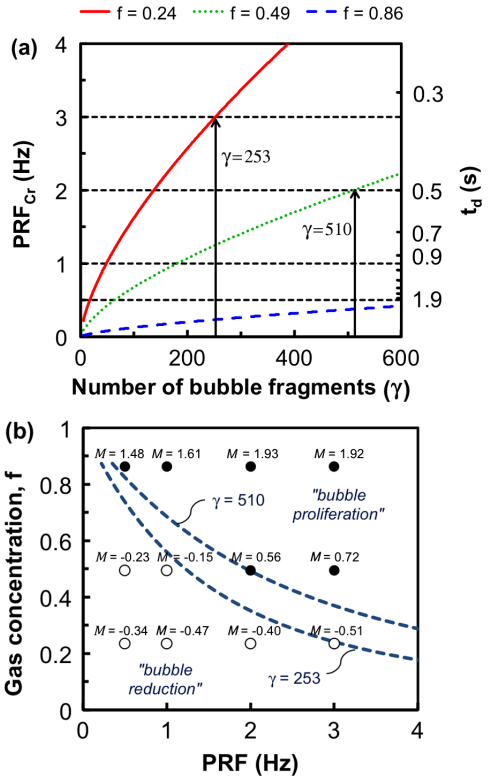


FIG. 6. (a) Plot of bubble-dissolution time $t_d$ and the threshold value $\text{PRF}_{\text{cr}} = 1/t_d$ versus $\gamma$ at gas concentration $f = 0.24$ (solid line), 0.49 (dotted line), and 0.86 (dashed line). Horizontal dashed lines at 0.5, 1.0, 2.0, and 3.0 Hz indicate experimental conditions. Vertical arrows point to the minimum ($\gamma = 253$) and maximum ($\gamma = 510$) number of daughter bubbles that cause our model to align with the experimental observations. (b) Comparison of bubble-dissolution model results with experimental data. Two dashed curves representing $\gamma = 253$ and 510 separate the regions of bubble proliferation (filled circles, $M > 0$) and reduction (open circles, $M < 0$).

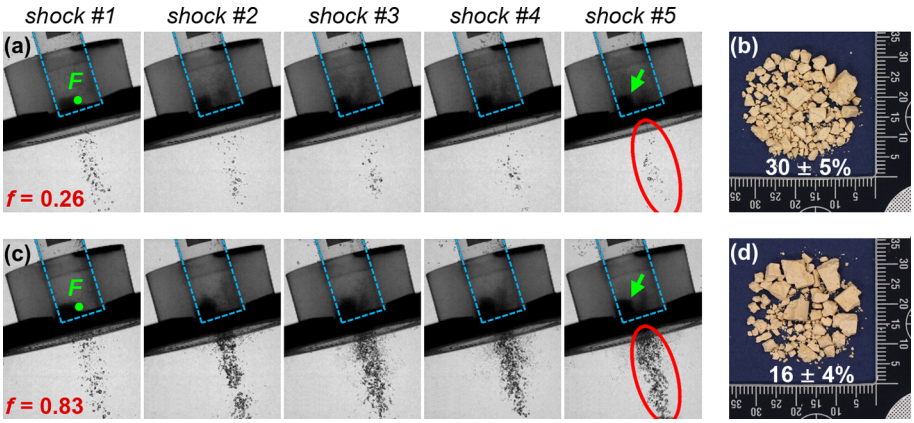


FIG. 7. (a),(c) High-speed images (40-$\mu$s exposure time) of maximum cavitation activity ($t = 250$ $\mu$s) around the stone holder (25-mm inner diameter, shown with dashed line) for five consecutive shocks and (b),(d) resultant stone fragments after 250 lithotripter shocks ($p_+ = 41$ MPa at the focus $F$, PRF $= 1$ Hz) in degassed (a),(b) and nondegassed (c),(d) water. Fragmentation efficiency (determined by the percent of fragments $< 2.0$ mm) is $30\% \pm 5\%$ in degassed water ($f = 0.26$, bubble reduction) compared to $16\% \pm 4\%$ in tap water ($f = 0.83$, bubble proliferation). Nondegassed tap water is used in the stone holder in both cases; the stone location is shown with an arrow. The circled regions in the fifth frame show bubble reduction (a) and bubble proliferation (c).

greater than 2 Hz, then bubble proliferation would not take place at this set of conditions. With this reasoning, $\gamma$ at which $f = 0.49$ crosses the $\mathrm{PRF_{cr}} = 2$ Hz line is the maximum $\gamma(= 510)$ that would cause our dissolution model to align with experimental observations.

By using these two observations, we can say that, for our dissolution model to align with our experimental observations, the value of $\gamma$ must fall in a range between 253 and 510 of equal-sized spherical daughter bubbles.

To compare the theoretical results to the experimental results, the $\mathrm{PRF_{cr}}$ curves for $\gamma = 253$ and $\gamma = 510$ are plotted in Fig. 6(b). For any values of $\gamma$ in the range [253:510], the theory predicts bubble reduction and bubble proliferation consistent with experimental observation. This prediction is indicated by $M < 0$ (shown above the corresponding point of the experimental condition) for all experimental cases below the range of $\gamma$ and $M > 0$ for those conditions above the range.

This figure is also useful in that it shows the gas concentration as a function of $\mathrm{PRF_{cr}}$ and provides guidance for choosing conditions for the stone comminution experiments presented in the next section. It will be shown that the conditions that fall into the region denoted as "bubble proliferation" lead to lower stone comminution than the conditions that fall into the region dubbed "bubble reduction."

## VI. STONE COMMINUTION RESULTS

Stone comminution efficiency is evaluated under two water conditions: one condition allowing for efficient wave transmission (degassed water, $f = 0.26$) and one which has substantial attenuation due to bubble proliferation (filtered tap water, $f = 0.83$). A PRF of 1 Hz is used for both of these conditions. The fragmentation efficiency (i.e., weight of fragments $< 2$ mm in diameter normalized by initial stone weight) is $30\% \pm 5\%$ in degassed water compared to $16\% \pm 4\%$ in tap water ($p = 0.002$ for a two-tailed student $t$ test with the 95% confidence level). Figures 7(b) and 7(d) show stones treated by using the degassed and nondegassed coupling medium, respectively. Stones treated by using degassed water break into noticeably smaller fragments than those treated by using nondegassed water, indicating better stone comminution. Additionally, imaging of the resultant bubble cloud in the beam path shows bubble reduction [circled in Fig. 7(a)] and bubble proliferation observed [circled in Fig. 7(c)]. The results show the effects of bubble proliferation on stone comminution for an *in vitro* setup.

## VII. DISCUSSION

In this study, we explore the influence of gas concentration and PRF on cavitation activity in the beam path and tensile wave attenuation. Two competing effects (bubble reduction and proliferation) are observed and are associated with tensile wave attenuation (Fig. 4). It is found that when bubbles proliferate there is a high attenuation of the rarefaction wave as shown in Figs. 2(a) and 2(c) and by the inverse relationship in Fig. 4. Measurements show a transmission of pressure impulse of only $T = 0.13$ for the case that exhibits the greatest proliferation of bubbles [Fig. 3(a), PRF $= 3$ Hz, $f = 0.86$, $M = 1.8$] but transmission of $T = 1.10$, a marginal increase in the pressure impulse, for the case that exhibits the greatest bubble reduction [Fig. 3(c), PRF $= 3$ Hz, $f = 0.24$, $M = -0.5$]. The attenuation of the rarefaction wave may be explained

by the tensile energy used to induce cavitation in the beam-path prefocally; in each cavitation event, a portion of the tensile energy of the rarefaction wave is used to expand a bubble. The marginal intensification of the tensile wave when a reduction of bubbles occurs can be explained with the same mechanism; if there are fewer cavitation nuclei and thus fewer cavitation events, there will be less loss in tensile energy to bubble expansion. It is interesting to note that in Fig. 4 all the cases fall on a single curve. This result suggests that there is a direct relationship between the depletion of tensile energy and the number of bubbles formed regardless of the water condition, operating condition, and mechanism that initiate the bubbles. Therefore, we can postulate that tensile attenuation is primarily due to the presence of cavitation bubbles and therein a consequence of the expansion of bubbles in the beam path.

Efficient transmission of the tensile wave may lead to increased cavitation in the vicinity of the stone causing more stone damage. Results from *in vitro* stone comminution experiments support this argument and suggest that when bubbles proliferate in the beam path [Fig. 7(a)] the fragmentation efficiency is compromised ($16\% \pm 4\%$ versus $30\% \pm 5\%$). However, the bubble cloud dynamics may not be comparable from the first five shocks (pressure measurement experiments) to the first 250 shocks (stone comminution experiments); for longer treatments, significant stirring may occur that could introduce bubble nuclei into the beam path. Additionally, in using an *in vivo* setup, we would not be able to control the gas concentration in the beam path, and thus our stone comminution results may not be repeatable *in vivo*. Furthermore, our *in vitro* setup does not utilize a coupling cushion, and it is hard to determine how much cavitation-related attenuation would occur in the balloon compared to other areas within the beam path, where the pressure is much higher. Related issues involve tensile attenuation due to bubbles in the coupling gel [31], bubble accumulation inside of the balloon, flow recirculation in the coupling medium [18], and acoustic streaming, which all can have an effect on bubble proliferation and tensile attenuation which may alter our experimental results.

Efficient transmission of the rarefaction wave occurs when there is minimal bubble activity in the beam path. To ensure that a lithotripter is being operated in a range where bubble proliferation does not occur, we identify the threshold for which bubble reduction transitions to proliferation *in vitro*. This threshold is determined by examining the mechanism hypothesized by Sapozhnikov *et al.* in Ref. [11] to be responsible for bubble proliferation, namely, the bubble-dissolution time relative to the shock period. If bubbles persist between shocks, then there will be a proliferation of bubbles, because the remaining bubble remnants will seed subsequent cavitation events during the passage of the next shock [9]. By varying the gas concentration in our experiments, we are able to modulate the dissolution time and thus align our experimentally determined bubble-proliferation threshold (function of the PRF and $f$) to a simple model of bubble dissolution (function of $f$ and $\gamma$). This alignment allows for the estimation of the unknown parameter $\gamma$, the number of daughter bubbles produced upon the collapse of a larger lithotripter bubble.

The primary unknown in our dissolution model is the number $\gamma$ and size distribution of daughter bubbles. After assuming that the sizes are uniform, the parameter $\gamma$ remains. The range of daughter bubbles that align our experimental observations with the model is between $\gamma = 253$ and 510 [Fig. 6(b)]. However, this range is obtained from several assumptions. It is more sensible to instead claim we have obtained an order of magnitude of $\gamma \sim 10^2$ for the number of daughter bubbles produced after collapse. This order of magnitude agrees with observations by Pishchalnikov, Williams, and McAteer [16], who observe $\gamma$ on the order of $10$–$10^2$ via the use of high-speed imaging of a single lithotripter bubble upon collapse. Previous work by Church and Flynn [32] suggests a range of $\gamma = 4$–$50$; however, this number is for a substantially smaller initial bubble driven by pulsed ultrasound. Moreover, the number and size distribution of daughter bubbles may be different for a collapse in a dense cloud compared to that of an isolated bubble.

In addition to the assumption of uniform daughter bubbles, several other simplifying assumptions to the model have also been made. The main assumptions are the following: the dissolution time is that of a single bubble in quiescent fluid; the daughter bubbles are spherical; the mass of daughter bubbles equals the mass of noncondensable gas taken into the bubble upon its initial expansion; and the relevant far-field gas concentration seen by the dissolving bubbles is the background concentration of the medium as prepared. Each of these assumptions limits both the applicability and the predictability of the model.

For example, because of acoustic streaming, buoyancy, and jetting upon collapse, the bubbles are not in a completely quiescent fluid [28].

In the case of a sparse bubble cloud (cases of bubble reduction) the assumption of a single bubble may be accurate, but as the cloud becomes more dense (cases of bubble proliferation) the single-bubble assumption is less useful.

Spherical daughter bubbles may be a valid assumption once the bubbles have stabilized and the only significant dynamic process is the diffusion of noncondensable gas back into the fluid.

The noncondensable gas assumption is likely valid in determining the mass of the daughter bubbles, because the residual vapor in the daughter bubbles after collapse condenses rapidly at the wall in comparison to the dissolution time of the bubble. Additional support for this assumption is shown in previous studies of bubble dynamics that show that, at the late stage of the bubble

lifetime, the mass of air is much greater than the mass of vapor [10,29].

Finally, with regard to the relevant gas concentrations seen by the bubbles, if the daughter bubbles are sufficiently far apart with respect to their small size, as they should be soon after formation, the relevant gas concentration surrounding the bubbles should closely match that of the far field. However, in a dense bubble cloud there may also be bubble-wall and bubble-bubble interactions [10] resulting in bubble surface instabilities (see the Appendix).

Though the model has some limitations, it does successfully provide an explanation consistent with the described experiments; moreover, it captures the threshold between bubble proliferation and reduction for reasonable values of $\gamma$, as can be seen by the two $\mathrm{PRF_{cr}}$ curves in Fig. 6(b). Yet, to develop an accurate model, many of the assumptions outlined above need to be revisited. For example, the assumption of equal daughter-bubble size is limiting, because the dissolution time is highly dependent on bubble size. Future work should include measurements of the parameter $\gamma$ and the daughter-bubble size distribution. Even with all the simplifications, the model does illustrate a mechanism that may determine whether bubble reduction or proliferation will occur and therefore when tensile attenuation will occur *in vitro*. Also, the model presented is differentiated from the work in Ref. [11] in which bubble fragmentation is not accounted for in the calculation of bubble-dissolution time. This estimate of the number of daughter bubbles $\gamma$ provides insight into the bubble dynamics in the beam path during SWL.

## VIII. CONCLUSIONS

The experimental findings on tensile attenuation do not directly transpose to *in vivo* treatment; however, we still systematically provide an explanation for bubble proliferation as it depends on gas concentration and the PRF and show its implications on tensile attenuation and on *in vitro* stone comminution. Also, we develop a simple model of bubble dissolution that accounts for fragmentation. For numbers of daughter bubbles consistent with previous experiments [16], the bubble-dissolution model is consistent with the bubble-proliferation experiments we show and hence provides insight into the bubble dynamics in the beam path during shock-wave lithotripsy.

## ACKNOWLEDGMENTS

This work is supported by the National Institutes of Health through Grants No. R37-DK052985-18 and No. S10-RR16802 and by the National Science Foundation Graduate Research Fellowship Program (S. F. and J. L.). The authors acknowledge the technical assistance of Neal Simmons in constructing the water degassing system.

## APPENDIX: SINGLE-BUBBLE FISSION

Bubble proliferation can be instigated by bubble surface instability due to a shear flow around a moving bubble. The criterion of bubble fragmentation can be obtained from theoretical consideration of Kelvin-Helmholz instability described by the Weber number

$$\mathrm{We} = \frac{2R_0\rho v^2}{\sigma}, \tag{A1}$$

where $R_0$ is the bubble radius, $v$ is the bubble translational velocity, $\rho$ is the density of water, and $\sigma$ is the surface tension of water [33]. If the Weber number is greater than the critical value of $\mathrm{We_{cr}} = 2\pi$, than the surface instability will develop and the bubble will split to produce multiple fragments with smaller radius $r_0$ to satisfy the criterion of stability, i.e.,

$$\mathrm{We_{cr}} \geq \frac{2r_0\rho v^2}{\sigma}. \tag{A2}$$

In a typical case $\mathrm{We} \approx 27$ [34], and, hence, the number of fragments can be estimated by

$$\gamma \propto \frac{{R_0}^3}{{r_0}^3} \geq \left(\frac{\mathrm{We}}{\mathrm{We_{cr}}}\right)^3 \approx 79. \tag{A3}$$

The Weber number strongly depends on the bubble translational velocity, which may reach the maximum of about 100 m/s upon bubble collapse [35]. The translational velocity also increases as the distance from a rigid boundary decreases; e.g., more daughter bubbles are expected near a kidney stone. The Weber number can be determined by the bubble interactions and external pressure in a bubble cluster and warrant further study.

[1] Y. A. Pishchalnikov, J. A. McAteer, and J. C. Williams, Jr., Effect of firing rate on the performance of shock wave lithotriptors, BJU International **102**, 1681 (2008).

[2] J. J. Rassweiler, T. Knoll, K. U. Kohrmann, J. A. McAteer, J. E. Lingeman, R. O. Cleveland, M. R. Bailey, and C. Chaussy, Shock wave technology and application: An update, European Urology **59**, 784 (2011).

[3] P. Zehnder, B. Roth, F. Birkhauser, S. Schneider, R. Schmutz, G. N. Thalmann, and U. E. Studer, A prospective randomised trial comparing the modified HM3 with the MODULITH (R) SLX-F2 lithotripter, European Urology **59**, 637 (2011).

[4] E. Yilmaz, E. Batislam, M. Basar, D. Tuglu, C. Mert, and H. Basar, Optimal frequency in extracorporeal shock wave lithotripsy: Prospective randomized study, Urology **66**, 1160 (2005).

[5] M. Liebler, T. Dreyer, and R. E. Riedlinger, Modeling of interaction between therapeutic ultrasound propagation and cavitation bubbles, Ultrasonics **44**, e319 (2006).

[6] J. A. McAteer, M. R. Bailey, J. C. Williams Jr, R. O. Cleveland, and A. P. Evan, Strategies for improved shock wave lithotripsy, Minerva Urol. Nefrol. **57**, 271 (2005).

[7] B. R. Matlaga and M. J. Semins, How to improve results with extracorporeal shock wave lithotripsy, Ther. Adv. Urol. **1**, 99 (2009).

[8] M. J. Semins, B. J. Trock, and B. R. Matlaga, The effect of shock wave rate on the outcome of shock wave lithotripsy: A meta-analysis, J. Urol. **179**, 194 (2008).

[9] Y. A. Pishchalnikov, O. A. Sapozhnikov, M. R. Bailey, I. V. Pishchalnikova, J. C. Williams, and J. A. McAteer, Cavitation selectively reduces the negative-pressure phase of lithotripter shock pulses, Acoust. Res. Lett. Online **6**, 280 (2005).

[10] W. Kreider, L. A. Crum, M. R. Bailey, and O. A. Sapozhnikov, Observations of the collapses and rebounds of millimeter-sized lithotripsy bubbles, J. Acoust. Soc. Am. **130**, 3531 (2011).

[11] O. A. Sapozhnikov, V. A. Khokhlova, M. R. Bailey, J. C. Williams, Jr., J. A. McAteer, R. O. Cleveland, and L. A. Crum, Effect of overpressure and pulse repetition frequency on cavitation in shock wave lithotripsy, J. Acoust. Soc. Am. **112**, 1183 (2002).

[12] R. E. Apfel, Acoustic cavitation inception, Ultrasonics **22**, 167 (1984).

[13] Y. A. Pishchalnikov, J. A. McAteer, I. V. Pishchalnikova, J. C. Williams, M. R. Bailey, and O. A. Sapozhnikov, *Bubble Proliferation in Shock Wave Lithotripsy Occurs during Inertial Collapse in Nonlinear Acoustics Fundamentals and Applications* (AIP, New York, 2008).

[14] R. K. Zeman, W. J. Davros, B. S. Garra, and S. C. Horii, Cavitation effects during lithotripsy. Part I. Results of in vitro experiments, Radiology **177**, 157 (1990).

[15] P. Huber, K. Jochle, and J. Debus, Influence of shock wave pressure amplitude and pulse repetition frequency on the lifespan, size and number of transient cavities in the field of an electromagnetic lithotripter, Phys. Med. Biol. **43**, 3113 (1998).

[16] Y. A. Pishchalnikov, J. C. Williams, and J. A. McAteer, Bubble proliferation in the cavitation field of a shock wave lithotripter, J. Acoust. Soc. Am. **130**, EL87 (2011).

[17] M. Arora, C. D. Ohl, and D. Lohse, Effect of nuclei concentration on cavitation cluster dynamics, J. Acoust. Soc. Am. **121**, 3432 (2007).

[18] J. Lautz, G. Sankin, and P. Zhong, Turbulent water coupling in shock wave lithotripsy, Phys. Med. Biol. **58**, 735 (2013).

[19] A. Henglein, D. Herburger, and M. Gutierrez, Sonochemistry: Some factors that determine the ability of a liquid to cavitate in an ultrasonic field, J. Phys. Chem. **96**, 1126 (1992).

[20] M. Strasberg, Onset of ultrasonic cavitation in tap water, J. Acoust. Soc. Am. **31**, 163 (1959).

[21] J. Colt, *Solubility of Atmospheric Gases in Freshwater* (Elsevier, London, 2012), Computation of Dissolved Gas Concentration in Water as Functions of Temperature, Salinity and Pressure, second ed.

[22] J. I. Iloreta, Z. Yufeng, G. N. Sankin, Z. Pei, and A. J. Szeri, Assessment of shock wave lithotripters via cavitation potential, Phys. Fluids **19**, 086103 (2007).

[23] N. Smith, G. N. Sankin, W. N. Simmons, R. Nanke, J. Fehre, and P. Zhong, A comparison of light spot hydrophone and fiber optic probe hydrophone for lithotripter field characterization, Rev. Sci. Instrum. **83**, 014301 (2012).

[24] E. Esch, W. N. Simmons, G. Sankin, H. F. Cocks, G. M. Preminger, and P. Zhong, A simple method for fabricating artificial kidney stones of different physical properties, Urol. Res. **38**, 315 (2010).

[25] X. Giannakopoulos, A. Evangelou, V. Kalfakakou, E. Grammeniatis, I. Papandropoulos, and K. Charalambpoulos, Human bladder urine oxygen content: Implications for urinary tract diseases, International urology and nephrology **29**, 393 (1997).

[26] M. A. Margulis, Kinetics of the number of cavitation bubbles in an ultrasonic field, Sov. Phys. Acoust. **22**, 145 (1976).

[27] I. Akhatov, O. Lindau, A. Topolnikov, R. Mettin, N. Vakhitova, and W. Lauterborn, Collapse and rebound of a laser-induced cavitation bubble, Phys. Fluids **13**, 2805 (2001).

[28] M. Arora, L. Junge, and C. D. Ohl, Cavitation cluster dynamics in shock-wave lithotripsy: Part 1. Free field, Ultrasound Med. Biol. **31**, 827 (2005).

[29] T. J. Matula, P. R. Hilmo, B. D. Storey, and A. J. Szeri, Radial response of individual bubbles subjected to shock wave lithotripsy pulses in vitro, Phys. Fluids **14**, 913 (2002).

[30] P. S. Epstein and M. S. Plesset, On the stability of gas bubbles in liquid-gas solutions, J. Chem. Phys. **18**, 1505 (1950).

[31] Y. A. Pishchalnikov, J. S. Neucks, R. J. VonDerHaar, I. V. Pishchalnikova, J. C. Williams, Jr., and J. A. McAteer, Air pockets trapped during routine coupling in dry head lithotripsy can significantly decrease the delivery of shock wave energy, J. Urol. **176**, 2706 (2006).

[32] H. G. Flynn and C. C. Church, A mechanism for the generation of cavitation maxima by pulsed ultrasound, J. Acoust. Soc. Am. **76**, 505 (1984).

[33] R. I. Nigmatulin, *Mathematical Modeling of Bubbly Liquid Motion and Hydrodynamical Effects in Wave Propagation Phenomena in Mechanics and Physics of Bubbles in Liquids* (Martinus Nijhoff, Hague, 1982).

[34] G. N. Sankin, in *Proceedings of the XIII Session of the Russian Acoustical Society* (GEOS, Moscow, 2003).

[35] A. Vogel, W. Lauterborn, and R. Timm, Optical and acoustic investigations of the dynamics of laser-produced cavitation bubbles near a solid boundary, J. Fluid Mech. **206**, 299 (1989).